

# ***Pristine or Highly Defective? Understanding the Role of Graphene Structure for Stable Lithium Metal Plating***

Wei Liu<sup>a\*</sup>, Yuting Xia<sup>a</sup>, Wenwu Wang<sup>b</sup>, Yizhe Wang<sup>a</sup>, Jialun Jin<sup>a</sup>, Yungui Chen<sup>a,b\*</sup>, Eunsu Paek<sup>c</sup>, David Mitlin<sup>a,c\*</sup>

*a: Institute of New-Energy and Low-Carbon Technology, Sichuan University, Chengdu, Sichuan, China, 610065*

*b: College of Materials Science and Technology, Sichuan University, Chengdu, Sichuan, China, 610065*

*c: Chemical & Biomolecular Engineering and Mechanical Engineering, Clarkson University, Potsdam, NY, USA 13699*

*\* weiliu@scu.edu.cn, \*chenyungui@scu.edu.cn, \*dmitlin@clarkson.edu*

## **Abstract**

We are the first to examine the role of graphene host structure/chemistry in plating-stripping in lithium metal anodes employed for lithium metal batteries (LMBs). Structural and chemical defects are bad since highly defective graphene promotes unstable solid electrolyte interphase (SEI) growth. This consumes the FEC additive in the carbonate electrolyte and is correlated with rapid decay in CE and formation of filament-like Li dendrites. A unique flow-aided sonication exfoliation method is employed to synthesize "defect-free" graphene (df-G), allowing for a direct performance comparison with conventional reduced graphene oxide (r-GO). At cycle 1, the r-GO is better electrochemically wetted by Li than df-G, indicating that initially it is more lithiophilic. With cycling, the nucleation overpotential with r-GO becomes higher than with df-G, indicating less facile plating reactions. The df-G yields state-of-the-art electrochemical performance, with the post cycled metal surface being relatively-smooth and dendrite-free. Conversely, r-GO templates have CE rapidly degrade from the onset, with extensive dendrites after cycling. Severe SEI growth and associated FEC depletion with r-

This is the author manuscript accepted for publication and has undergone full peer review but has not been through the copyediting, typesetting, pagination and proofreading process, which may lead to differences between this version and the [Version of Record](#). Please cite this article as [doi: 10.1002/aenm.201802918](https://doi.org/10.1002/aenm.201802918).

GO are further confirmed by electrochemical impedance analysis (EIS) and surface science methods (XPS). We provide a new design rule for Li metal templates: An ideal host must be non-catalytic towards SEI formation *per se*.

**keywords:** liquid phase exfoliation (LPE); Sodium metal battery (SMB); solid electrolyte interphase (SEI), solid electrolyte interface (SEI), mossy dendrite.

## Introduction

Lithium ion batteries (LIBs) are ubiquitous for electric vehicles (EV) and portable electronics, and are making inroads into municipal and stationary energy storage applications.<sup>[1]</sup> Prevailing LIBs utilize graphite anodes as an intercalation host, yielding a practical capacities in the 330–430 mAh cm<sup>-3</sup> range, which is actually lower than the practical volumetric capacity of commercial cathodes including LiCoO<sub>2</sub> (550 mAh cm<sup>-3</sup>) and doped spinel LiM<sub>x</sub>Mn<sub>2-x</sub>O<sub>4</sub> (M=Ni, V, Cu).<sup>[2]</sup> Establishing new anode - cathode material combinations beyond the “rocking-chair” systems is necessary for further gains in cell energy, which in turn translate into longer automotive travel range, wider grid applications, etc.<sup>[3]</sup> Lithium metal battery systems (LMBs) are being sought as an ultimate replacement to LIBs, opening possibilities for much higher energy densities for the lithium metal anode possesses a high theoretical capacity (2,277 mAh/cm<sup>-3</sup>, 3860 mAh/g) and the 0 V vs. Li/Li<sup>+</sup> plating plateau.<sup>[4]</sup> This gives LMBs high energy, especially when coupled with a high capacity cathode such as S, Se or S-Se.<sup>[4c, 4e, 4f, 5]</sup>

It is well-known that the stability of Li metal during extended charge - discharge cycling is extremely problematic. This is primarily due to its high reactivity with most liquid electrolytes and the large volume changes associated with deposition - dissolution (volume change is infinite only if the entire electrode is dissolved and re-precipitated).<sup>[6]</sup> In conventional carbonate electrolytes the solid electrolyte interphase (SEI) layer on metallic Li is unstable, exposing fresh metal surfaces to the electrolyte effectively at every cycle.<sup>[7]</sup> This has been classically associated with metal dendrite growth, which consumes both Li ions and liquid electrolyte, leading to the cell “drying out” even prior to electrical shorting. A qualitative scenario for SEI promoted dendrite growth is along the

following lines: A chemical and/or structural heterogeneity forms in the SEI, which results in a locally non-uniform Li flux to this “hot spot”, leading to preferred deposition of non-planar Li.<sup>[8]</sup> The protrusion is further accelerated by strong local electrical field and by now preferential ion flux, resulting in the formation of dendrites.<sup>[9]</sup> Thus localized rather than planar growth becomes self-amplified, and minute metal protrusions with cycling become full micron-scale dendrites. The dendrite may grow long enough to pierce the separator and catastrophically short the anode to the cathode. Else it will consume enough electrolyte and Li ions while growing more SEI around it to have the cell gradually fail by capacity fade.<sup>[10]</sup>

Tremendous effort has been devoted to address the Li dendrite problem. One strategy to stabilize the SEI layer and suppress Li dendrite growth is to employ electrolyte additives. These include fluoroethylene carbonate (FEC)<sup>[11]</sup>, fluorinated ether<sup>[12]</sup>, vinylene carbonate (VC)-lithium nitrate (LiNO<sub>3</sub>)<sup>[13]</sup>, Cs<sup>+</sup> and Rb<sup>+</sup> salts<sup>[14]</sup>, Li-fluoride (LiF)<sup>[15]</sup>, Li-polysulfide<sup>[16]</sup> and Li-nitrate<sup>[17]</sup> *etc.* However, if the SEI is unstable, such electrolyte additives may be consumed during repeated cycling, indicating that this solution is not fully effective by itself.<sup>[18]</sup> Another key emerging strategy is to employ electrically conductive secondary supports/templates/ protection layers (in addition to the Cu current collector) to control Li plating and stripping behavior. Such supports may offer “hosting”, confining the volume expansion of the Li metal within a compliant buffering matrix. The supports may also offer “templating”, reducing the local current density by effectively increasing the available surface area for metal nucleation. The supports could also offer “protection”<sup>[19]</sup>, by effectively acting as an ion permeable separator that minimizes new Li metal - electrolyte interfaces. A well-designed host may offer all these benefits: controlling the volume expansion to be in favorable directions, dispersing the plating/stripping current, serving as dense template for crystallite nucleation, and stabilizing the electrolyte interface. The conductive support approach is well suited to be employed in conjunction with the additives approach, potentially offering synergistic performance.

Owing to inherent advantages such as excellent electrical and ionic conductivity, potential ease of processing and cost-effectiveness, carbon-based supports with tailored structures and morphologies have been investigated. These include Super P<sup>[20]</sup>, graphene<sup>[21]</sup>, graphene oxide<sup>[22]</sup>, N-doped graphene,<sup>[23]</sup> graphitic foam<sup>[24]</sup>, graphitic micro-tube<sup>[25]</sup> *etc.* Due to its open 2D structure, inherent stability against corrosion, and excellent electrical and thermal conductivity, graphene and many of

its  $sp^2$  bonded analogues are among the most popular carbon supports studied. Graphene defects (including heteroatoms, nanopores, vacancies, topological defects, *etc.*) are considered “lithiophilic” sites to help Li-metal wet the carbon host, especially when melt-infusion method is employed to thermally introduce a Li reservoir.<sup>[21d, 23, 26]</sup> However, these defect sites were previously recognized to catalyze electrolyte reduction, i.e. formation of SEI<sup>[27]</sup>. Therefore, the critical open questions for the Li metal community are the following: In sum, are graphene (or more generally carbon) chemical and structural defects beneficial or deleterious for Li metal supports? What is the ideal “hosting”, “templating” and/or “protection” carbon for Li metal?

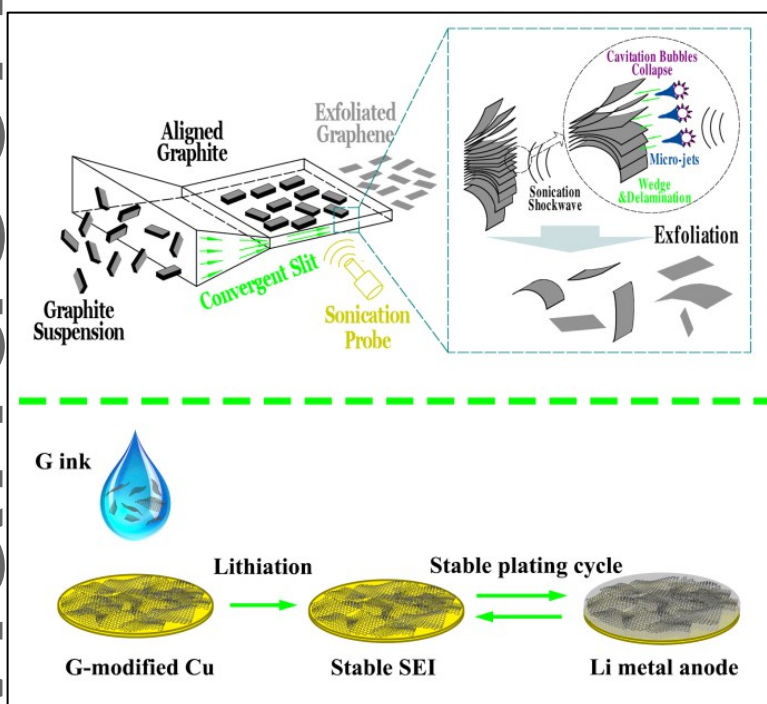
Here we conclusively address these important and interrelated questions. We are the first to demonstrate that graphene defects are actually quite deleterious for efficient Li deposition and subsequent stripping, being directly correlated with low Coulombic efficiency (CE) and with irregular dendritic growth of the Li metal front. It is demonstrated that defective graphene, as opposed to “defect-free” graphene, promotes copious solid electrolyte interphase (SEI) formation at cycle 1 and afterward. The thick and dynamically growing SEI may be reasonably concluded to be a key cause of the observed instability, a process which becomes self-amplified with cycling as the growing SEI exhausts the electrolyte additives designed to stabilize it.

## **Result and Discussion**

### ***Synthesis and Properties of df-G and r-GO***

Ultrasonic cavitation has been employed to yield graphene materials from graphite, the approach being known as the liquid-phase-exfoliation (LPE) method<sup>[28]</sup>. The cavitation bubbles in the suspension implode at the liquid-solid interface of the working material. This transient implosion will focus significant acoustic energy onto the solid, the phenomena being termed “micro-jets”. The micro-jets lead to extreme and highly localized conditions, where temperatures of 5000 K and pressures of hundreds of bars have been predicted.<sup>[29]</sup> The violence of the process will also generate highly reactive species in the solution, including radicals from sonolysis of the solvent vapor.<sup>[29b, 29c]</sup> For materials with highly anisotropic bonding, such as graphite or various sulfides, ultrasonic

sonication will lead to extensive exfoliation along the van der Waals bonded planes. The micro-jets could also directly break the  $sp^2$  bonds along (002) of graphite, fracturing/scissoring the material in-plane and leading to various graphene defects such as di-vacancies, Stone Wales defects and nanopores.<sup>[30]</sup> Introduction of surface and edge-site O and OH moieties (hydroxyl, carboxyl, epoxy, etc.) have also been reported<sup>[31]</sup>.



**Schematic 1.** top: Illustration of the flow exfoliation process, giving preferential alignment of flowing graphite particles relative to the shock wave. Inset : Schematic illustration of the exfoliation process for "defect-free" graphene (df-G). bottom: Illustration on the use of df-G to promote a stable metal growth front.

If the micro-jets can be preferentially directed normal to the graphite edges rather than normal to the basal plane, the weak out of plane bonding in (002) may be used to form sheets of highly pristine defect-free graphene. Due to a spontaneous random orientation of graphite flakes in a liquid medium, an anisotropic ultrasonic treatment is not possible in a static condition. However, it is known that disk-like particles are prone to align along the flow with respect to the strain velocity distribution due to elongation or/and shear strain<sup>[32]</sup>. A self-designed slit-flow was adopted here to achieve such alignment accordingly. Governed by rheological laws, the suspended graphite platelets can be induced to align along the flow with respect to the slit geometry when flowing through the

slits (enlarged insets in Figure S1). When flowing through the convergent slit, due to local shear distribution the suspended graphite platelets can be induced to align along the flow with respect to the slit geometry<sup>[32a, 32b]</sup>. Simultaneous to the pump-driven cyclic flowing of suspension, sonication shockwave was imposed to the aligned particles with propagation direction parallel to the oriented graphite platelets. This flow-aided sonication (FAS) process will align the graphite precursor flakes parallel to the sonication wave to focus the energy on the flake edges. This efficiently exfoliates the graphite flakes while minimizing structural damage to the basal planes or introducing oxidation. Additional details for fabrication of "defect-free" graphene (df-G), including a reactor schematic (**Fig. S1**) and graphite and suspension properties (**Fig. S2**), are provided in the Electronic Supplementary Information (ESI).

Conventional Hummer's method based on the well-known oxidation-reduction route was employed to synthesize reduced graphene oxide (r-GO). As shown in the text below, the morphology, defectiveness and oxygen content of the fabricated r-GO agreed well with literature<sup>[33]</sup>. To quantitatively examine the role of graphene structure on Li metal plating, df-G and r-GO supports were fabricated by drop-casting the graphene dispersions onto commercial Cu foils, without any binder or conductive filler. The mass loading of the supports was identical in each case, being about 0.4 mg/cm<sup>2</sup>. The top half of **Scheme 1** illustrates the FAS exfoliation process and the general mechanism for producing df-G. The bottom half of the schematic is an illustration of the df-G and r-GO support fabrication process.

**Figure 1** shows the morphology and structure of "defect-free" graphene df-G and reduced graphene oxide r-GO. The df-G is shown on the top panels while the r-GO is shown on the bottom panels. **Figure 1(a)** shows atomic force microscopy (AFM) analysis of df-G. Height maps associated with the line scans of five individual sheets are overlaid with the AFM image. The apparent height of monolayer graphene as probed by AFM is known to be in the range from 0.8 - 1.5 nm, depending on the substrate, tip and measurement parameters, *etc.*<sup>[28b, 34]</sup> The five df-G sheets that were analyzed were all approximately 1.5 nm, indicating that they are either monolayer or bi-layer graphene structures. A pore-free monolayer of graphene should have a true surface area of 2630 m<sup>2</sup>/g, a bi-layer would be in the 1300 m<sup>2</sup>/g range. Such surface areas are on-par or higher than most carbons employed for Li metal supports.<sup>[35]</sup> **Figures 1(b)** and **(c)** show transmission electron microscopy (TEM) analysis of df-G. **Figure 1(b)** shows a bright field micrograph a df-G flakes which is folded in sections.

From the overall morphology it may be observed that df-G still possesses the overall lateral morphology of the parent graphite flakes having a combination of angular and rounded edges. The SAD pattern and linear intensity profile map shown on Fig. 1(c) is consistent with (110) and (100) reflections for graphene oriented in the [001] zone axis, indicating highly crystalline nature of the graphene layers produced by FAS. A high resolution TEM (HRTEM) micrograph of df-G is shown in **Figure 1(d)**, with FFT pattern and FFT-filtered image shown as insets. The classical hexagonal FFT pattern and the associated honeycomb atomic arrangement of graphene are present, indicating the high orderliness of the structure with minimal defects in the basal plane.

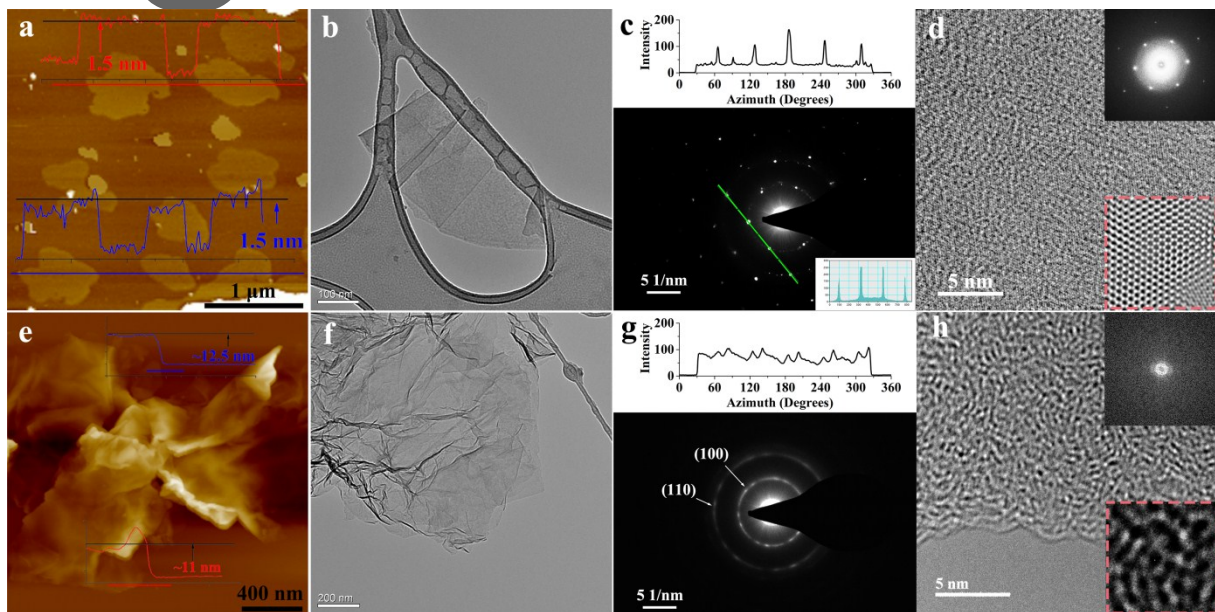


**Figure 1:** Morphology and structure of df-G (top) and conventional reduced graphene oxide r-GO (bottom). (a) AFM image and its height profile of df-G flakes deposited on mica; (b) and (c) TEM analysis of df-G, showing a bright field image, and representative electron diffraction (ED) pattern with a linear intensity profile along a row of reflections (green line), analysis of the intensity distribution of (100) diffraction along the Azimuth angle were shown at the top; (d) HRTEM lattice image of df-G. Inset: FFT pattern and FFT-filtered lattice image highlighting the highly ordered graphene lattice, with minimal defects. (e) AFM image and its height profile of r-GO flakes deposited on mica; (f) – (h) bright field TEM and SAD analysis of r-GO. The streaked rings in the ED pattern was indexed as (100) and (110), and (100) of r-GO shows low polarization degree along the Azimuth angle in contrast to df-G; (h) HRTEM lattice image of disordered r-GO. The FFT pattern and FFT-filtered lattice image demonstrate a highly defective structure with poor graphene plane alignment.

**Figures 1(e) - (i)** highlights the structure of r-GO. **Figure 1(e)** shows the AFM image and height maps. It may be observed that the r-GO graphene flakes exhibit a "ruffled" morphology that typical

for reduced graphene oxide materials found in literature.<sup>[4d,36]</sup> The flakes are microns in width. The AFM maps highlight the ruffled morphology of the sheets, showing exaggerated heights of 11 and 12.5 nm. In reality, the r-GO carbons are lower thickness although the true dimensions can't be obtained by AFM due to the wrinkling and aggregation. The BET analysis for r-GO, shown in Fig. S3 shows the material to possess Type III BET isotherms typical for reduced graphene oxide -type materials. The BET surface area was 507 m<sup>2</sup>/g, a cumulative pore volume of 1.61 cc/g, and a wide distribution of primarily mesopores were observed. This will become important for interpretation of the electrochemical findings, since nanopores in r-GO should be highly catalytic toward electrolyte decomposition and would become plugged with SEI below ~ 1 V vs. Li/Li<sup>+</sup>.<sup>[37]</sup>

Per the TEM results shown in **Figure 1(f)** the r-GO is ruffled and relatively spherical in its lateral dimensions. The SAD shows steaked (100) and (110) ring patterns. The significant disorder in r-GO is far different from the structure of df-G, as no distinct graphene crystal lattice is observable in the HRTEM images shown in **Figure 1(h)**. The observed high disorder of r-GO agrees with r-GO structures reported in literature<sup>[38]</sup>. Hummer's synthesized reduced graphene oxide is depicted as an amorphous matrix with nanocrystalline domains that contain residual oxygen groups, vacancies and topological defects.<sup>[38b, 39]</sup> Literature reported r-GO is almost always a mixture of sp<sup>2</sup> and sp<sup>3</sup> bonding.<sup>[38a, 38b]</sup>

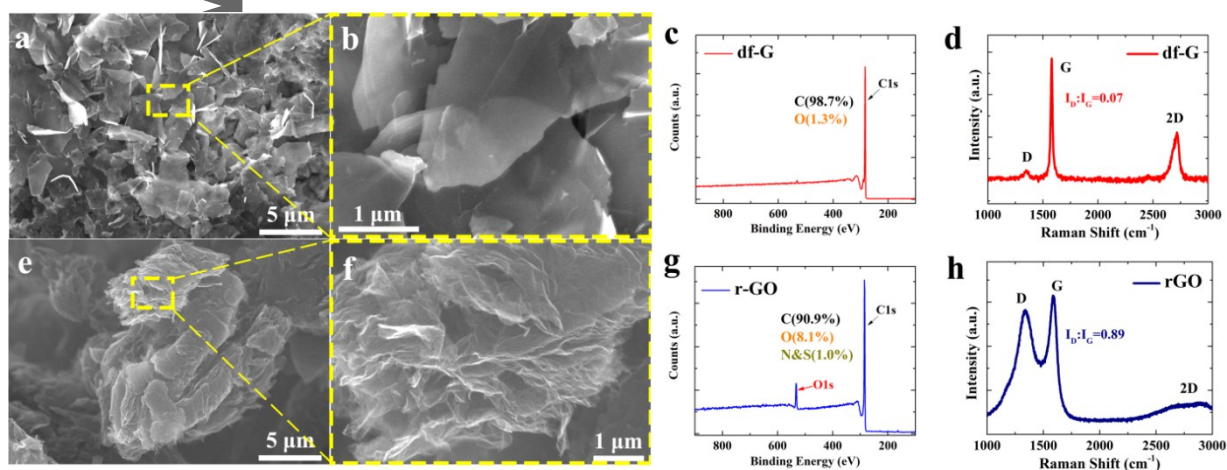


**Figure 2:** Morphology, near-surface chemistry and structure of df-G (top) and r-GO (bottom). a) and b) SEM micrograph of df-G deposited on the Cu foil current collector. c) Overview XPS overview spectra for df-G highlighting it uniquely low O content. Corresponding high resolution XPS peaks are shown in Figs. SX. d) Raman spectra highlighting the D to G band intensity ratio of 0.07 in df-G, being much lower than the corresponding 0.89 in r-GO. e) – h) highlight the same analysis for r-GO, showing it to be much rougher, much higher in surface O content and much more defective.

**Figure 2** shows the morphology of df-G and r-GO deposited on the Cu current collector and employed for the plating-stripping analysis shown later on. **Figure 2(a)** and **2(b)** shows df-G, while **Figs. 2(e)** and **2(f)** shown r-GO at identical magnifications. Since these two carbons possess different thickness and structure, the electrodes are qualitatively different when viewed top-down. Another key difference between df-G and r-GO is in their heteroatom content. X-ray Photoelectron Spectroscopy (XPS) was employed to investigate the near-surface chemistry of these two materials. XPS analysis of df-G is shown in **Fig. 2(c)** and **Fig. S4(a)**, suggesting that the graphene is free of impurities other than a trace amount of oxygen (1.3 at%). Conversely, per **Fig. 2(g)**, the r-GO possesses a much higher oxygen content (8.1 at%) and a discernable amount of S and N (1 at% total). The oxygen atoms in r-GO are mainly ascribed to residual oxygenated carbon groups (C-O/C=O), whereas df-G exhibits much lower functional group signals per the high resolution C 1s and O 1s spectra (**Fig. S4 (b ,c)**). The 1% N and S in r-GO is suspected to be introduced by sulfuric acid and nitrate from the synthesis process. Raman spectra shown in **Figs. 2(d)** and **(h)** further illustrates the structural difference between df-G and r-GO, in which a ratio between the D-band and the G-band can be employed to quantify the defectiveness of the carbon materials. This clearly reveals the highly ordered nature of df-G, showing an  $I_D/I_G$  ratio of 0.07. However, r-GO is much less ordered, showing an  $I_D/I_G$  ratio of 0.89. We note the complete lack of a 2D peak in r-GO, due to high levels of graphene disorder, agreeing with previous reports<sup>[33a, 33b, 38c]</sup>.

One can compare the structural and chemical features of df-G and r-GO versus representative graphene nanosheets exfoliated via a number of established methods in existing literature. This comparison is shown in **Table S1**<sup>[28a, 30b, 30c, 31, 33b, 34, 38b, 38c, 40]</sup>. The r-GO in the current study is similar in structure to prior reported r-GO. In fact, it possesses slightly lower defectiveness and heteroatom content compared to prior studies. To contrast, the df-G exhibits unique structural integrity with extremely low heteroatom content for a "wet" synthesized graphene material. Therefore r-GO and df-G constitute ideal model system for understanding templated Li plating.

### ***Intrinsic SEI Formation Tendency of df-G and r-GO***

The formation of a solid electrolyte interphase (SEI) is the irreversible reduction and chemical decomposition of the electrolyte in contact with the anode. Electrochemically, SEI formation is

manifested as irreversible capacity loss and impedance rise at voltages below approximately 1 V Li/Li<sup>+</sup>. This means that when a lithium metal battery is charged, SEI formation occurs even before plating begins. SEI formation process involves reduction of the solvent molecules to Li<sub>2</sub>O or Li<sub>2</sub>CO<sub>3</sub>, Li alkyl carbonates and Li alkoxides, all of which irreversibly consume active Li. The reported early (e.g. cycle 1 - 3) Coulombic efficiency (CE) values for a wide range of carbon materials is often lower than 50%.<sup>[41]</sup> It is also recognized that structural and chemical defects in a carbon will catalyze SEI formation on its surface.<sup>[27]</sup> For instance, when more disordered graphitic carbons were tested as lithium ion battery (LIB) anodes, the CE loss and impedance rise at cycle 1 was worse<sup>[42]</sup>. Also, SEI was recently found to be thicker at the heteroatoms sites in a nitrogen-doped carbon.<sup>[43]</sup> What is still yet to be understood, however, is how structural and chemical defects affect the metal plating/stripping behavior when analogous carbons are employed as a Li metal plating host.

We first tested df-G and r-GO between 3 - 0.01 V vs. Li/Li<sup>+</sup>. This corresponds to a typical lithium ion battery (LIB) anode testing protocol, with the lower voltage cutoff being above the equilibrium Li plating potential. We adopted these tests to compare intrinsic SEI formation on df-G and r-GO, without the influence of plated Li metal - electrolyte interaction that would drive additional extensive SEI growth. Galvanostatic results for carbon Li/Li<sup>+</sup> half-cells are shown in **Figs. 3(a)** and **3(b)**. They indicate that df-G and r-GO possess distinctly different "high voltage" SEI formation properties: The first cycle irreversible capacity loss of r-GO reached 1863 mA/g, whilst that of df-G was only at 148 mAh/g. This initial capacity loss is primarily due to SEI formation on the carbon surfaces. Moreover, as can be seen from **Fig. 3(c)**, the ongoing cycling behavior df-G and r-GO is very different, with distinct voltage profiles. The df-G has a reversible capacity of 525 mAh/g, which is almost half that of r-GO. The difference in the shapes of the voltage profiles is synonymous with Li being reversibly stored in structural and heteroatom defects in r-GO, while intercalation being favored in df-G.<sup>[42a, 44]</sup> Per **Figs. 3(d)** and **3(e)**, the CE in df-G is quickly stabilized with cycling, going from 78% at cycle 1 to near 100% at cycle 2 and afterward. Conversely the cycling CE for r-GO is 35% at cycle 1, with CE never going above 95% in the first 10 cycles. This indicates that the SEI layer on the much more defective r-GO remains unstable, an observation which will be key for explaining the 0 V Li/Li<sup>+</sup> plating performance.

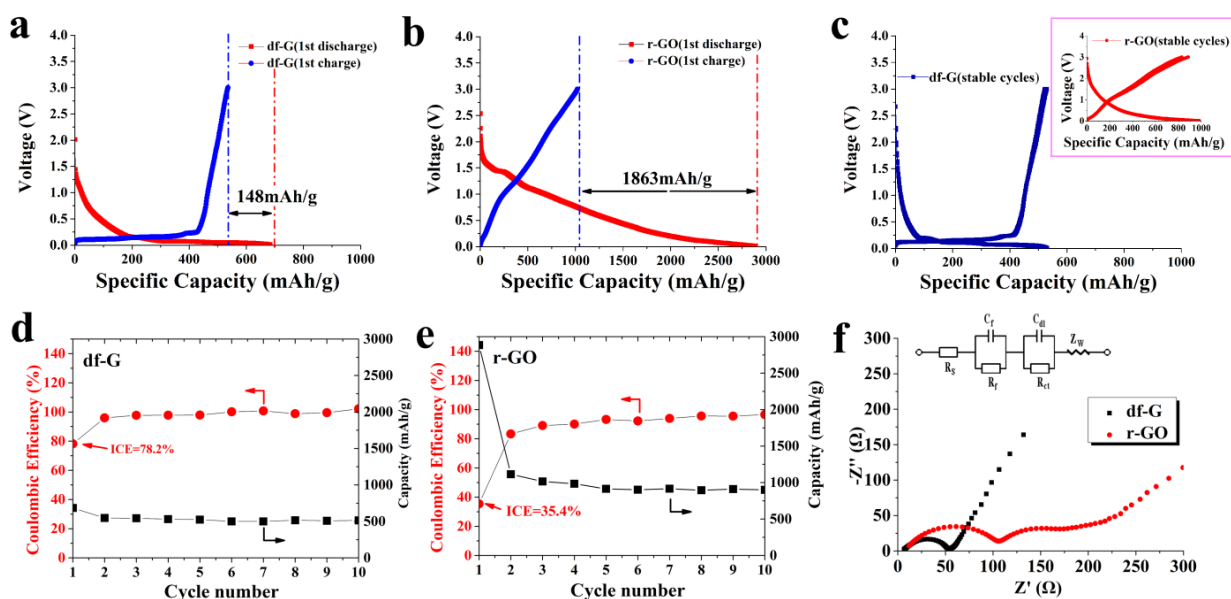


**Figure 3:** (a) and (b) Cycle 1 charge - discharge behavior of df-G and r-GO, respectively. Electrodes were tested in the high voltage range 2.5 - 0.01 V vs. Li/Li<sup>+</sup>, at 100 mA/g. The lower voltage cutoff is significantly above the equilibrium Li plating potential of 0 V. (c) Steady -state cycling behavior of df-G, with r-GO as an insert. (d) and (e) Cycling Coulombic efficiency (CE) and reversible capacity for df-G and r-GO, respectively. Electrochemical impedance analysis (EIS) Nyquist plots of df-G and r-GO after cycle 1, highlighting the major difference in R<sub>SEI</sub>.

This major difference in SEI formation propensity was further verified by electrochemical impedance spectroscopy (EIS), the Nyquist plot being shown in **Fig. 3(f)** (equivalent circuit models shown in the inset). A frequency range 0.1 Hz ~1 MHz with an AC amplitude of 5 mV was employed. For Li ion storage, the EIS tests were conducted at terminal lithiation voltage at cycle 1. The df-G exhibits impedance behavior that is well fit by a single arc model. However, a double arc impedance model is needed to fit the Nyquist plots for r-GO. This key difference is attributable to the much higher SEI-related surface film impedance (R<sub>SEI</sub>) of r-GO, which is large enough to be distinguishable from the charge transfer resistance (R<sub>CT</sub>).

**Table 2.** Fitted EIS values for AES-G and IPS-G electrodes after the initial galvanostatic discharge vs. Li/Li<sup>+</sup>.

Sample	R <sub>s</sub>	R <sub>ct</sub>	R <sub>f</sub> (R <sub>SEI</sub> )
--------	----------------	-----------------	------------------------------------

df-G	6.19 $\Omega$	43.7 $\Omega$ ( $R_{ct} + R_{SEI}$ )	
r-GO	8.9 $\Omega$	94 $\Omega$	80 $\Omega$

### Comparison of df-G and r-GO as Li Metal Host

Now that the intrinsic SEI formation tendency of df-G versus r-GO is discussed, we can examine their efficacy for stable reversible Li plating and stripping near 0 V vs. Li/Li<sup>+</sup>. As indicated earlier, the mass loading of the supports employed for plating reactions is 0.4 mg/cm<sup>2</sup>, an order of magnitude lower than what is typically employed for Li ion storage anodes. Prior to the Li metal plating/stripping testing (0 V, theoretical), the cells were "conditioned" by cycling several times at 100 mA/g through a voltage range of 0.01V - 3V vs. Li/Li<sup>+</sup>, leaving the electrodes at 0.01 V vs. Li/Li<sup>+</sup>. This process stabilized the carbon structure, largely eliminating any ambiguity from its contribution to early cycling irreversible capacity.<sup>[44-45]</sup> Current density of 0.5, 1, 2 and 4 mA/cm<sup>2</sup> and 30 minutes deposition time were employed for the plating studies, corresponding to a total capacity of 0.25, 0.5, 1 and 2 mAh/cm<sup>2</sup>. Since no "extra" reservoir of Li was used on the working electrode and the CE was less than 100%, the anodic voltage increased to the upper set limit of 1 V vs. Li/Li<sup>+</sup> at every delitiation.

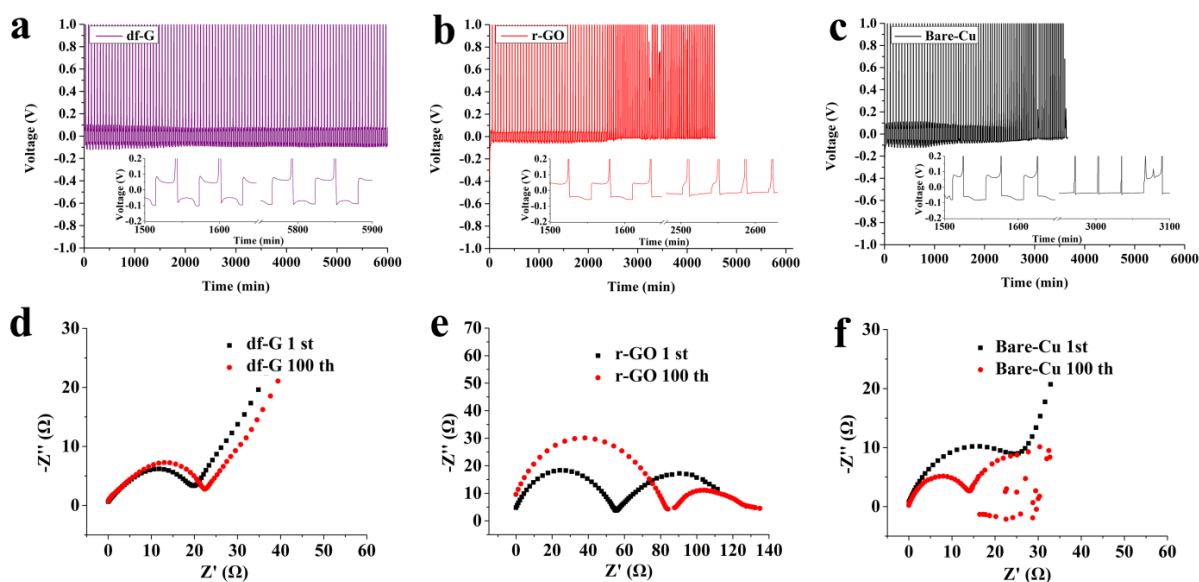


**Figure 4:** Electrochemical plating-stripping behavior and EIS Nyquist plots df-G (a, d), r-GO (b, e) and bare Cu (c, f). Samples were tested at 2 mA/cm<sup>2</sup> for 30 minutes per cycle.

**Figure 4** compares the plating/stripping voltage profiles for the df-G, r-GO, and the bare Cu foil which was used as a baseline. Current densities of  $2 \text{ mA/cm}^2$  and 30 min deposition time were adopted, corresponding to capacity of  $1 \text{ mAh/cm}^2$  at each plating/stripping cycle. The foil covered by df-G demonstrates far superior plating/stripping cycle stability among the three systems. The voltage profiles for df-G remain relatively stable throughout the test regime. Conversely, with r-GO severe voltage fluctuations are present after 3000 min of cycling. Voltage fluctuation instability, indicative of an unstable Li metal front, occur with the baseline bare Cu as well. Occasional voltage drops were observed in r-GO and with Cu, which may be ascribed to intermittent "soft-shorts" leading to mixed electronic - ionic conduction. Once more SEI has grown, the fine dendrites would lose their electrical conductivity path due to the associated volume changes, and the system would go back to pure ionic conduction through the electrolyte. We did not investigate soft shorting with r-GO and Cu in detail, the core point being that the df-G electrode does not display this phenomenon.

EIS analysis was conducted after plating/stripping cycle 1 and cycle 100. For Li metal plating, the EIS tests were conducted at OCP to ensure equilibrium state of the cell. These Nyquist plots are shown in **Figs. 4(d), (e) and (f)**, with the associated fits being shown in **Table 3**. The charge transfer resistance  $R_{CT}$  in the fit accounts for the charge transfer resistances between the carbon host and Li and the resistance of SEI film - electrolyte interface. In fact, since the SEI is a complex composite of organic and inorganic phases, there are multiple internal interfaces within the SEI itself that contribute to that semicircle. The r-GO has by far higher  $R_{CT}$  and  $R_{SEI}$  both at cycle 1 and cycle 100, confirming the major difference in the SEI levels right from the start of testing. Importantly after 100 cycles,  $R_{SEI}$  for r-GO further increases ( $\sim 26\%$ ), while the value for df-G remains stable. The impedance spectra of bare Cu had a single arc which did not allow for deconvolution into  $R_{CT}$  vs.  $R_{SEI}$ . Due to the much lower surface area available for Li plating of the planar bare Cu current collector, a direct comparison with df-G and r-GO is not appropriate.

**Table 3.** Fitted EIS values for df-G, r-GO and baseline Cu electrodes after 1<sup>st</sup> and 100<sup>th</sup> plating/stripping cycles.

Sample	$R_s$	$R_{ct}$	$R_{SEI}$
df-G 1 <sup>st</sup>	4.7 $\Omega$	8.0 $\Omega$	9.5 $\Omega$
df-G 100 <sup>th</sup>	12.8 $\Omega$	10.1 $\Omega$	10.0 $\Omega$
r-GO 1 <sup>st</sup>	3.28 $\Omega$	73.8 $\Omega$	57.2 $\Omega$
r-GO 100 <sup>th</sup>	4.47 $\Omega$	50.8 $\Omega$	85.3 $\Omega$
Bare-Cu 1 <sup>st</sup>	7.8 $\Omega$	27.8 $\Omega$ ( $R_{ct} + R_{SEI}$ )	
Bare-Cu 100 <sup>th</sup>	unable to analyze, shorted?		

Recent exciting studies report a connection between “lithiophilicity” of the template and the chemistry of the carbon supports<sup>[21d, 23]</sup>. In electrochemical terms, the lithiophilicity is manifested as a lower plating overpotential. In our case, we too observed a difference in the initial overpotential for the nominally lithiophilic template of r-GO versus a less lithiophilic template of df-G. This is illustrated in **Fig. 5(a)**. At cycle 1, the lowest plating overpotential is for r-GO (-0.1 V vs. Li/Li<sup>+</sup>), as compared to df-G (-0.18 V) and to bare Cu (-0.2 V). This is consistent with previous reports that chemical defects such as OH groups will serve as lithiophilic sites<sup>[22]</sup>. Dramatically, in the subsequent cycles, the r-GO and the df-G display an opposite trend. In **Fig. 5(b)** cycles 1 - 10 are shown. By cycle 2, the r-GO actually gives a larger plating overpotential, which increases further with higher cycle number. Above cycle 20 the r-GO and the bare Cu overpotential becomes unstable per the reasons described earlier, while df-G remains stable. A straight-forward explanation for this trend is that with increasing cycle number there is more SEI formed around the r-GO host. During the anodic Li stripping, the working electrode is fully delithiated (no Li reservoir is employed), but the SEI layer

largely remains in place. The remnant SEI then acts as a kinetic barrier to facile Li plating during the next cathodic scan, driving the increase in the overpotential.

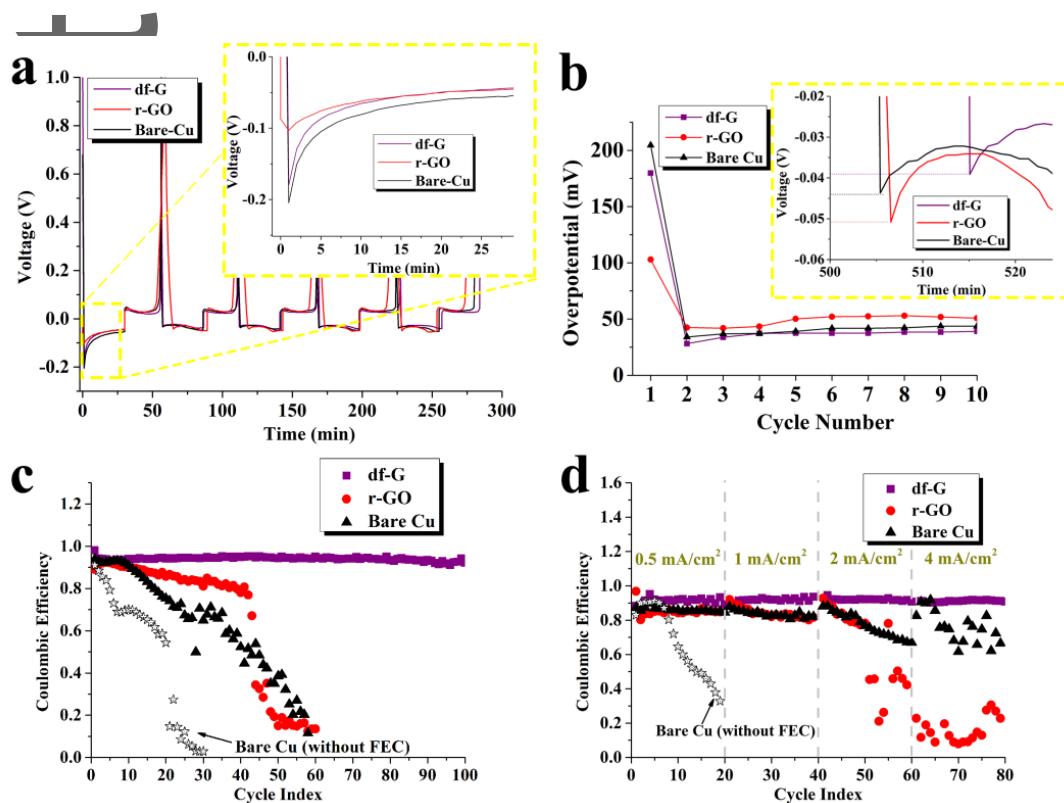


**Figure 5:** (a) A comparison of the voltage profiles for df-G, r-GO and bare Cu for first several plating-stripping cycles at  $0.5\text{mA}/\text{cm}^2$ , with the inset showing cycle 1 Li metal nucleation potential; (b) overpotential as a function of cycle number at  $0.5\text{mA}/\text{cm}^2$ , inset showing the cycle 10<sup>th</sup> Li metal nucleation potential; (c, d) Plating – stripping CE at  $2\text{ mA}/\text{cm}^2$  and at various current densities, respectively.

As can be seen in **Fig. 5(c)** only df-G can undergo stable plating/stripping cycles with CE at 94% and higher. The df-G template offers intrinsically stable interfaces for uniform electrochemical plating/stripping reactions, leading to dendrite-free surface morphology (shown in next set of figures). Conversely, both r-GO and bare Cu exhibit fast CE decay. Per **Fig. 5(d)**, the df-G host allows for plating current densities up to  $4\text{ mA}/\text{cm}^2$  without appreciable CE loss. Conversely, even higher CE decay is observed with both r-GO and bare Cu when current densities are increased to  $2\text{ mA}/\text{cm}^2$ . We ascribe the superior performance of df-G to a more stable SEI, which consumes less active Li, less electrolyte and importantly less fluoroethylene carbonate (FEC). It is known that FEC will have a positive effect on Li metal cycling efficiency by stabilizing the surface morphology. This is directly

correlated with the SEI structure. With FEC, the SEI layer on Li surface was more mechanically stable and more effective in suppressing further parasitic reactions, leading to a more uniform and compact Li deposit.<sup>[46]</sup> Due to the higher reactivity of FEC, greater amounts of LiF and  $\text{Li}_x\text{PF}_y$ <sup>[11a]</sup>, as well as higher portion of the reduction products of cyclic carbonate or polycarbonate species<sup>[11b]</sup> are present in the SEI. We note the key role of FEC in promoting an initially robust SEI structure in bare Cu; significantly improved CE was observed for the bare Cu electrode with FEC as compared to Cu without it (another baseline). These FEC-free Cu results are shown in **Figs. 5(c, d)** as well. To be effective, FEC has to be incorporated into the SEI. If more SEI continues to grow, the limited amount of FEC in the electrolyte (5vol.%, representative of most studies) will become depleted. With r-GO, since SEI growth is ongoing, FEC exhaustion is likely to be the case as well.

**Figure 6** shows top-down SEM micrographs after the samples have undergone 100 cycles, showing the materials in the plated state. Li metal deposited on the bare Cu foil is shown in **Figs 6(g) and (h)**. Coarse filament-like dendrite morphologies with branches having diameters of several microns are observed, being consistent with previous studies on bare Cu.<sup>[47]</sup> It is expected that preferential Li metal deposition on geometrical perturbances and defects in the Cu current collector will initiate non-planar growth. The geometric and chemical heterogeneity of the pre-existing SEI layer on the Cu will further amplify the Li front growth instability.<sup>[48]</sup> The role of the graphene chemical and structural defectiveness in promoting stable Li plating may be further understood by comparing **Figs. 6 (a, b)** for df-G versus **(d, e)** for r-GO. **Figs. 6 (c, f, i)** show schematic cross-sections of the post-cycled electrodes. The df-G specimen exhibits relatively uniform Li metal topography, while that of r-GO is classically dendritic with numerous filament-like dendrites taken as synonymous with tip growth.<sup>[49]</sup>

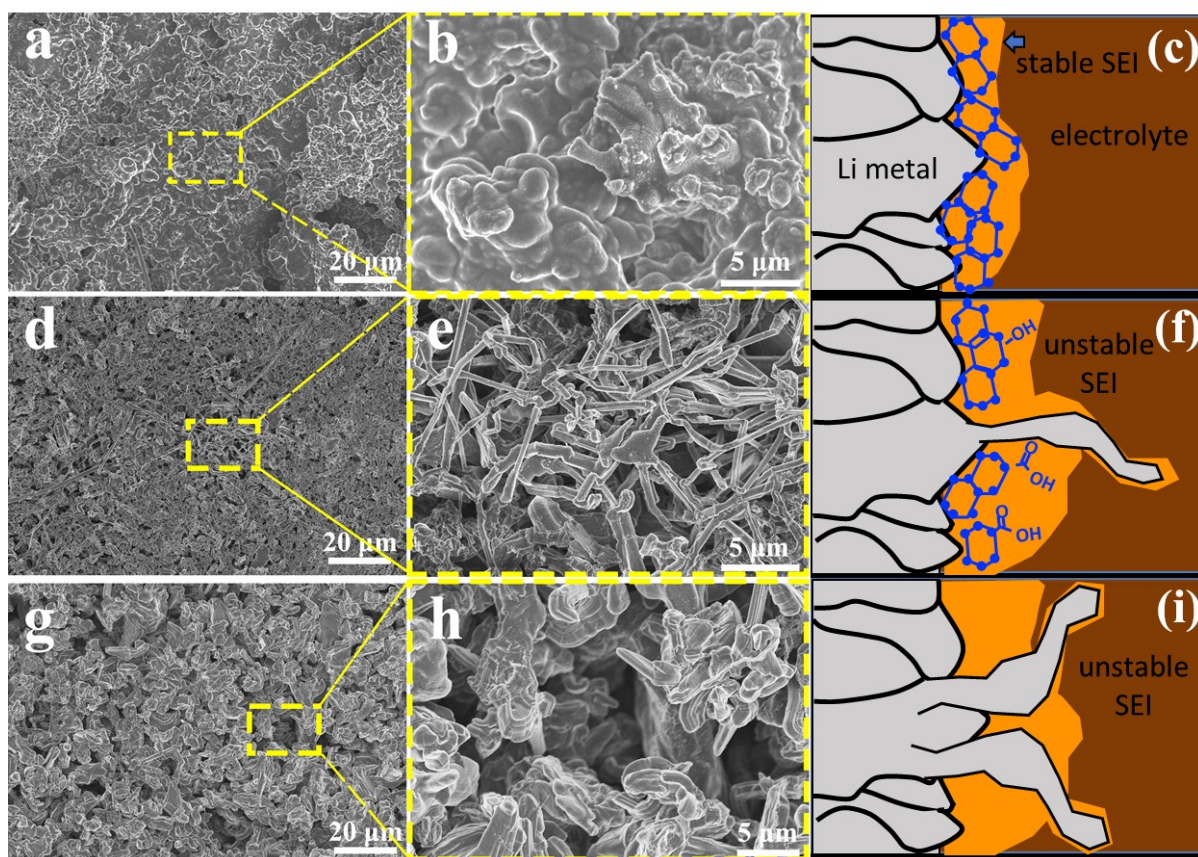


**Figure 6.** Top-down SEM micrographs of the post-100 cycles electrode surfaces in the fully plated condition (a,b) df-G, (d,e) r-GO and (g,h) baseline Cu. Schematics of the SEI formation process and the role of defect-free or highly defective graphene is shown to their right in (c, f, i).

The Li accessible surface area in df-G and r-GO electrodes should be sufficient to promote dense metal nucleation in both cases. Therefore, the tremendous difference in plating/stripping behavior and in the post-cycled electrode surfaces is not just an effective current density issue. The key difference in the two graphenes is their structural and chemical defectiveness which correlates to their intrinsic propensity to grow SEI. For the Li to plate on any electrically conductive current collector, it first has to ionically diffuse through the electrically insulating SEI layer. A thicker and potentially less homogeneous SEI will lead to non-uniform Li ion conduction through it. The Li ion flux will vary according to SEI phase and local thickness, selectively depositing metal on “hot-spots” to form protrusions. With cycling, these protrusions will advance by tip growth (likely) through the path of least resistance within the heterogeneous SEI. In other words, both the Li ions going in and the Li metal going out will be non-uniform. The SEI-growth driven exhaustion of the FEC additive

would make this effect worse, leading to self-amplification in the instability of the Li interface for the r-GO and Cu specimens. On the contrary, the initially thinner SEI formed on df-G will remain stable during cycling since the FEC added to the electrolyte would not be exhausted. A lower cathodic overpotential with df-G during cycling means that there is a lower nucleation barrier with this host. A classic result of nucleation thermodynamic analysis is that an increased nucleation barrier energy favors heterogeneous nucleation<sup>[50]</sup>. This means that the observed higher overpotential in r-GO due to more severe SEI formation will intrinsically promote less uniform Li deposition *per se*.

A recent highly exciting study has demonstrated a counterintuitive fact that pristine monolayer graphene grown on a Cu current collector will actually promote Li dendrites.<sup>[51]</sup> This was shown to be due to the poor wetting and hence large nuclei size of the plating metal on the low energy (002) graphene surface. Conversely, important early and recent works highlighted that materials such as hexagonal BN, graphene, r-GO and expanded graphene suppress dendrite growth when the Li deposits nucleate underneath the layers, next to the current collector.<sup>[21d, 26, 52]</sup> Knowing this key difference (promoted dendrites with Li on top, suppressed dendrites with Li beneath) leads us to conclude that df-G acts as a metal host. Lithium nuclei form in the free space between the Cu current collector and deposited df-G layers, which shields the metal from reacting with the electrolyte. This is also the likely scenario with r-GO, except in that case the graphene host itself drives the excessive SEI formation through electrolyte interaction with its structural and chemical defects.

Keeping in mind the critical role of SEI film in determining the electrochemical reversibility, we carried out SEM and XPS analysis of the SEI layer formed on the plated Li metal surfaces. The df-G and r-GO samples analyzed have undergone 100 plating-stripping cycles and were left in the fully plated state. **Figure S5** shows analysis of the SEI formed on the deposited Li metal with the df-G electrode. **Figure S5(a)** shows the SEM image and the associated energy-dispersive X-ray spectroscopy (EDXS) elemental-maps of C, O and F. The F element associated with LiF is uniformly distributed throughout the electrode surface. **Figures S5(b-d)** show the high-resolution C 1s, F 1s and Li 1s XPS spectra. As may be seen in XPS results, the C 1s, F 1s and Li 1s spectra fit well with the three Li compounds classically associated with SEI: LiF, Li<sub>2</sub>CO<sub>3</sub> and ROCO<sub>2</sub>Li.<sup>[13a, 53]</sup> The uniform F signal

throughout the electrode surface is indicative of a homogeneous distribution of LiF, which forms by the decomposition of FEC.

**Figure S6** shows the same analysis for the r-GO electrode. **Figure S6(a)** shows the SEM image and the associated EDXS elemental-maps of C, O and F. **Figures S6(b-d)** show the high-resolution C 1s, F 1s and Li 1S XPS spectra. Enriched regions of F element, indicated by arrows, correspond well with the most severe topographical features of the plated surface. These LiF-rich deposits are correlated with dendrite tips, which indicates that FEC preferentially decomposes in these regions. FEC is known to become incorporated into the growing SEI through the formation of an inorganic ion-permeable LiF layer. This in-turn stabilizes the SEI structure for both lithium ion battery and lithium metal battery anodes<sup>[11a, 11b, 46, 54]</sup>. One could then argue that the enhanced F signal corresponds to regions where SEI growth was catalyzed, *i.e.* at dendrite tips and at structural/chemical defects in the r-GO. As more SEI is formed in those regions, additional LiF becomes incorporated there as well. The localized F-rich areas on the Li metal surfaces with r-GO but not with df-G support the argument that defects accelerate SEI formation and ultimate FEC exhaustion. **Figure S7** directly compares the relative intensity of the XPS spectra for the SEI layer formed on the post-cycled metal deposits. The F:O atomic ratio may be regarded as a semi-quantitative measure for the relative content of LiF versus O-compounds within the top ~ 6 nm of the SEI (probe depth limit of XPS signal). In df-G, the F:O atomic ratio is 1.2, while in r-GO the F:O atomic ratio is 0.47. This further corroborates cycling-induced FEC exhaustion with r-GO. The relative intensity of the F vs. O peaks goes down as FEC becomes exhausted while  $\text{Li}_2\text{CO}_3$ ,  $\text{ROCO}_2\text{Li}$  etc. keep growing.

Finally, it is important to point out that while the defective r-GO might be unfavorable from a Li metal plating perspective, it is still highly useful as a primary Li ion storage anode. For example, if one were to set a cut off 30 or 40 mV vs.  $\text{Li}/\text{Li}^+$ , then metal plating will no longer be thermodynamically favorable. The specific capacity of the r-GO electrode will then far exceed that of defect-free graphene (df-G). In that regard, various forms of reduced graphene oxide and similarly defective carbons are still highly advantageous as anode materials for Li-ion batteries. Such is widely reported in scientific literature and the current findings do not disagree with this general conclusion.

## Conclusions

We examine the critical role of graphene structure and chemistry in promoting efficient plating-stripping in lithium metal anodes employed for lithium metal batteries (LMBs). We are the first to demonstrate that graphene defects are extremely deleterious for stable plating-stripping cycling since a defective carbon surface promotes copious solid electrolyte interphase (SEI) formation, which in turn is directly linked to Li metal dendrite growth. Highly defective graphene promotes unstable solid electrolyte interphase (SEI) growth, which in turn consumes the fluoroethylene carbonate (FEC) additive, leading to a catastrophic self-amplification in the process. Unstable SEI growth is directly linked to the observed fast decay in plating/stripping Coulombic efficiency (CE) and to filament-like Li metal dendrites. A new flow-aided sonication exfoliation method is employed to exfoliate graphite into "defect-free" graphene (df-G), allowing for a direct performance comparison with conventional defective reduced graphene oxide (r-GO) and with a bare Cu current collector. The df-G is single-nm thick, highly ordered (Raman  $I_D/I_G = 0.07$ ) and pure (1.3 at.% O), this combination being unachievable by traditional sonication exfoliation methods. Agreeing with past studies, conventional r-GO is more disordered ( $I_D/I_G$  of 0.89) and oxygen-rich (14 at.% O). At cycle 1, the r-GO is better electrochemically wetted by Li than df-G, indicating that initially it is more lithiophilic. However, with cycling the Li nucleation overpotential of r-GO actually becomes higher than that of df-G, indicating less facile plating reactions. The df-G based Li plating template yields state-of-the-art electrochemical performance with the post-cycled metal surface being relatively smooth and dendrite-free. This is achieved in conventional carbonate electrolyte with 5 vol.% FEC as an additive. The r-GO templates provide much inferior cycling with cycling CE rapidly degrading from the onset, and the post-cycled electrodes displaying extensive filament-like dendrites. Extensive SEI growth on r-GO is further confirmed by electrochemical impedance analysis (EIS).

## Experimental Section

### *Materials Synthesis*

Extensive details of df-G and r-GO synthesis and analytical characterization of the materials are also provided in Electronic Supplemental Information (ESI). A photograph of the self-designed flow-aided sonication (FAS) apparatus is shown in **Figure S1**. The labels on the photograph are A) Flow channel with convergent-slit configuration; B) Sonication probe; C) Thermocouple; D) Flow pipe employing a peristaltic pump with arrows showing the flow direction; and E) Water bath. The

graphite is suspended in N-methyl-pyrrolidone (NMP) to form suspension. As a result of liquid shear, the graphite platelets in the suspension will align with respect to the flow direction. This is governed by a group of dimensionless parameters (Reynolds number  $R_e$ , Peclet number  $P_e$ , etc.), with detailed flow calculations provided in the ESI. A sonication probe was used to impose shockwaves to the flowing oriented graphite flakes in the suspension. For the flow aligned moving graphite flakes, the shockwave hits the flakes directly at their edge, rather than normal to their wide dimension, i.e. the basal plane. Following the FAS treatment, the suspension was centrifuged to isolate exfoliated graphene from the remnant graphite. Reduced graphene oxide r-GO sheets were prepared by the modified Hummer's method.<sup>[33b, 38c, 55]</sup>

### **Electrochemical Analysis**

Lithium plating templates were fabricated by drop-casting dispersion of df-G or r-GO onto a standard Cu foil current collector, without any binders or carbon black. Typical loading was 0.4 mg/cm<sup>2</sup> (0.01 mg resolution microbalance, AUW120D, SHIMADZU). To understand the SEI formation tendencies of both materials, Li storage (not plating) experiments were also performed. To clean the graphene from any residual solvent prior to cell assembly, the electrodes were heated at 400°C for 1h in an argon-filled tube-furnace. Lithium - graphene cells were assembled using 2025-type coin cells. Assembly was done in an argon-filled glovebox with O and H<sub>2</sub>O below 0.1 ppm. The Li metal foils were approximately 800 microns thick, purchased from China Energy Lithium Co., Ltd. A standard research-grade electrolyte of 1M LiPF<sub>6</sub> dissolved in 1:1:1 (volume ratio) mixture of ethylene carbonate (EC), ethyl methyl carbonate (EMC) and diethyl carbonate (DEC), with 5 vol.% FEC was used. Some baseline Cu current collector - Li metal cells were also tested without the FEC additive. All electrolyte chemicals were purchased from Energy Chemicals and employed in their as-received state. Cellgard 2400 was employed as separator. Lithium metal plating/stripping and storage experiments were done employing a LAND-CT2001A test system. Electrochemical impedance spectroscopy (EIS) analysis was performed with an AUTOLAB M204 (Metrohm, Switzerland). After 100 cycles the 2025 cells were disassembled in a glovebox and cleaned with diethyl carbonate (DEC). This removed the remaining electrolyte and any soluble SEI products, leaving behind an adherent coating of insoluble SEI on the plated Li metal. The dried electrodes were double protected in in argon filled seal bags placed inside argon filled screw-bottles, minimizing air exposure during transfer to the SEM.

## Supporting Information

Detailed experimental procedures, additional data is available from the Wiley Online Library or from the author.

## Acknowledgements

W.L. (conception of synthesis, performing experiments) acknowledges financial support from National Science Foundation of China (51702223), China Postdoctoral Science Foundation (2017M623028) and Young Scholar Start-up Grant of SCU (2017SCU12026). We would like to thank the Analytical & Testing Center of SCU for microscopy work and Prof. Wang Hui and Prof. Wang Shanling for their assistance in electron microscopy. D.M. and E.P. (conception and interpretation of electrochemical studies, manuscript preparation) are supported by the U.S. Department of Energy, Office of Basic Energy Sciences, Division of Materials Sciences and Engineering under Award # DE-SC0018074.

## References

- [1] S. Chu, A. Majumdar, *Nature* **2012**, *488*, 294.
- [2] N. Nitta, F. Wu, J. T. Lee, G. Yushin, *Mater. Today* **2015**, *18*, 252.
- [3] B. Scrosati, J. Hassoun, Y.-K. Sun, *Energy Environ. Sci.* **2011**, *4*, 3287.
- [4] a) W. Xu, J. Wang, F. Ding, X. Chen, E. Nasybulin, Y. Zhang, J.-G. Zhang, *Energy Environ. Sci.* **2014**, *7*, 513; b) D. S. Geng, N. Ding, T. S. A. Hor, S. W. Chien, Z. L. Liu, D. Wu, X. L. Sun, Y. Zong, *Adv. Energy. Mater.* **2016**, *6*, 14; c) J. Ding, H. Zhou, H. Zhang, L. Tong, D. Mitlin, *Adv. Energy. Mater.* **2018**, *8*, 1701918; d) X. Yao, N. Huang, F. Han, Q. Zhang, H. Wan, J. P. Mwizerwa, C. Wang, X. Xu, *Adv. Energy. Mater.* **2017**, *7*, 1602923; e) L. Li, S. Basu, Y. Wang, Z. Chen, P. Hundekar, B. Wang, J. Shi, Y. Shi, S. Narayanan, N. Koratkar, *Science* **2018**, *359*, 1513; f) M. Li, Z. Chen, T. Wu, J. Lu, *Adv. Mater.* **2018**, DOI: 10.1002/adma.201801190e1801190.

- [5] a) Z. Li, J. Zhang, H. B. Wu, X. W. Lou, *Adv. Energy. Mater.* **2017**, *7*, 1700281; b) H. Xu, S. Wang, A. Manthiram, *Adv. Energy. Mater.* **2018**, *8*, 1800813.
- [6] a) G. Zheng, S. W. Lee, Z. Liang, H.-W. Lee, K. Yan, H. Yao, H. Wang, W. Li, S. Chu, Y. Cui, *Nat. Nanotechnol.* **2014**, *9*, 618; b) L. Li, S. Li, Y. Lu, *Chem. Commun.* **2018**, *54*, 6648.
- [7] D. Wang, C. Luan, W. Zhang, X. Liu, L. Sun, Q. Liang, T. Qin, Z. Zhao, Y. Zhou, P. Wang, W. Zheng, *Adv. Energy. Mater.* **2018**, *8*, 1800650.
- [8] C. Xin-Bing, Z. Rui, Z. Chen-Zi, W. Fei, Z. Ji-Guang, Z. Qiang, *Adv. Sci.* **2016**, *3*, 1500213.
- [9] J.-i. Yamaki, S.-i. Tobishima, K. Hayashi, S. Keiichi, Y. Nemoto, M. Arakawa, *J. Power Sources* **1998**, *74*, 219.
- [10] D. Wang, W. Zhang, W. T. Zheng, X. Q. Cui, T. Rojo, Q. Zhang, *Adv. Sci.* **2017**, *4*, 11.
- [11] a) Z. Xue-Qiang, C. Xin-Bing, C. Xiang, Y. Chong, Z. Qiang, *Adv. Funct. Mater.* **2017**, *27*, 1605989; b) E. Markevich, G. Salitra, F. Chesneau, M. Schmidt, D. Aurbach, *ACS Energy Lett.* **2017**, *2*, 1321; c) H. M. Kim, J.-Y. Hwang, D. Aurbach, Y.-K. Sun, *J. Phys. Chem. Lett.* **2017**, *8*, 5331.
- [12] C. Zu, N. Azimi, Z. Zhang, A. Manthiram, *J. Mater. Chem. A* **2015**, *3*, 14864.
- [13] a) J. Guo, Z. Wen, M. Wu, J. Jin, Y. Liu, *Electrochem. Commun.* **2015**, *51*, 59; b) C. Zu, A. Manthiram, *J. Phys. Chem. Lett.* **2014**, *5*, 2522.
- [14] F. Ding, W. Xu, G. L. Graff, J. Zhang, M. L. Sushko, X. Chen, Y. Shao, M. H. Engelhard, Z. Nie, J. Xiao, X. Liu, P. V. Sushko, J. Liu, J.-G. Zhang, *J. Am. Chem. Soc.* **2013**, *135*, 4450.
- [15] Y. Lu, Z. Tu, L. A. Archer, *Nat. Mater.* **2014**, *13*, 961.
- [16] S. Nanda, A. Gupta, A. Manthiram, *Adv. Energy. Mater.* **2015**, *0*, 1801556.
- [17] W. Li, H. Yao, K. Yan, G. Zheng, Z. Liang, Y.-M. Chiang, Y. Cui, *Nat. Commun.* **2015**, *6*, 7436.
- [18] a) R. Jung, M. Metzger, D. Haering, S. Solchenbach, C. Marino, N. Tsiouvaras, C. Stinner, H. A. Gasteiger, *J. Electrochem. Soc.* **2016**, *163*, A1705; b) R. Dugas, A. Ponrouch, G. Gachot, R. David, M. R. Palacin, J. M. Tarascon, *J. Electrochem. Soc.* **2016**, *163*, A2333; c) S. A. Webb, L.

- Baggetto, C. A. Bridges, G. M. Veith, *J. Power Sources* **2014**, *248*, 1105; d) S. S. Zhang, *Electrochim. Acta* **2012**, *70*, 344.
- [19] S. Suresh, Z. P. Wu, S. F. Bartolucci, S. Basu, R. Mukherjee, T. Gupta, P. Hundekar, Y. Shi, T.-M. Lu, N. Koratkar, *ACS Nano* **2017**, *11*, 5051.
- [20] H. K. Kang, S. G. Woo, J. H. Kim, S. R. Lee, Y. J. Kim, *Electrochim. Acta* **2015**, *176*, 172.
- [21] a) Z. Rui, C. Xin - Bing, Z. Chen - Zi, P. Hong - Jie, S. Jia - Le, H. Jia - Qi, W. Jinfu, W. Fei, Z. Qiang, *Adv. Mater.* **2016**, *28*, 2155; b) X.-B. Cheng, H.-J. Peng, J.-Q. Huang, R. Zhang, C.-Z. Zhao, Q. Zhang, *ACS Nano* **2015**, *9*, 6373; c) A. Zhamu, G. Chen, C. Liu, D. Neff, Q. Fang, Z. Yu, W. Xiong, Y. Wang, X. Wang, B. Z. Jang, *Energy Environ. Sci.* **2012**, *5*, 5701; d) R. Mukherjee, A. V. Thomas, D. Datta, E. Singh, J. Li, O. Eksik, V. B. Shenoy, N. Koratkar, *Nat. Commun.* **2014**, *5*, 3710.
- [22] F. Tara, S. F. A., Y. Vitaliy, S.-A. Soroosh, D. Ramasubramonian, H. Zhennan, R. Ramin, M. Farzad, B. P. B., S.-Y. Reza, *Adv. Funct. Mater.* **2018**, *28*, 1705917.
- [23] Z. Rui, C. Xiao - Ru, C. Xiang, C. Xin - Bing, Z. Xue - Qiang, Y. Chong, Z. Qiang, *Angew. Chem. Int. Ed.* **2017**, *56*, 7764.
- [24] J. Song, X. Sen, W. Linjun, D. Zhenzhen, C. Lina, C. Jiafeng, K. Xianghua, G. Ming, L. Junling, Z. Yanwu, J. Hengxing, R. R. S., *Adv. Mater.* **2016**, *28*, 9094.
- [25] J. Song, S. Zhaowei, G. Yali, Q. Zhikai, G. Chengkun, K. Xianghua, Z. Yanwu, J. Hengxing, *Adv. Mater.* **2017**, *29*, 1700783.
- [26] D. Lin, Y. Liu, Z. Liang, H.-W. Lee, J. Sun, H. Wang, K. Yan, J. Xie, Y. Cui, *Nat. Nanotechnol.* **2016**, *11*, 626.
- [27] a) P. Verma, P. Maire, P. Novák, *Electrochim. Acta* **2010**, *55*, 6332; b) E. Peled, S. Menkin, *J. Electrochem. Soc.* **2017**, *164*, A1703.
- [28] a) Y. Hernandez, V. Nicolosi, M. Lotya, F. M. Blighe, Z. Sun, S. De, I. T. McGovern, B. Holland, M. Byrne, Y. K. Gun'Ko, J. J. Boland, P. Niraj, G. Duesberg, S. Krishnamurthy, R. Goodhue, J. Hutchison, V. Scardaci, A. C. Ferrari, J. N. Coleman, *Nat. Nano.* **2008**, *3*, 563; b) C. Backes, T.

- M. Higgins, A. Kelly, C. Boland, A. Harvey, D. Hanlon, J. N. Coleman, *Chem. Mater.* **2017**, *29*, 243; c) A. Ciesielski, P. Samorì, *Adv. Mater.* **2016**, *28*, 6030.
- [29] a) Y. Tomita, A. Shima, *Destructive Action of Cavitation Bubbles Collapsing Near Boundaries*, Springer Berlin Heidelberg, Berlin, Heidelberg **2003**; b) K. S. Suslick, J. J. Gawienowski, P. F. Schubert, H. H. Wang, *J. Phys. Chem.* **1983**, *87*, 2299; c) K. S. Suslick, J. J. Gawienowski, P. F. Schubert, H. H. Wang, *Ultrasonics* **1984**, *22*, 33.
- [30] a) Y. Y. Huang, T. P. J. Knowles, E. M. Terentjev, *Adv. Mater.* **2009**, *21*, 3945; b) M. V. Bracamonte, G. I. Lacconi, S. E. Urreta, L. E. F. Foa Torres, *J. Phys. Chem. C* **2014**, *118*, 15455; c) A. Ciesielski, S. Haar, A. Aliprandi, M. El Garah, G. Tregnago, G. F. Cotella, M. El Gemayel, F. Richard, H. Sun, F. Cacialli, F. Bonaccorso, P. Samorì, *ACS Nano* **2016**, *10*, 10768; d) F. Hennrich, R. Krupke, K. Arnold, J. A. Rojas Stütz, S. Lebedkin, T. Koch, T. Schimmel, M. M. Kappes, *J. Phys. Chem. B* **2007**, *111*, 1932; e) Y. Y. Huang, T. P. J. Knowles, E. M. Terentjev, *Adv. Mater.* **2009**, *21*, 3945.
- [31] a) E. Y. Polyakova, K. T. Rim, D. Eom, K. Douglass, R. L. Opila, T. F. Heinz, A. V. Teplyakov, G. W. Flynn, *ACS Nano* **2011**, *5*, 6102; b) T. Skaltsas, X. Ke, C. Bittencourt, N. Tagmatarchis, *J. Phys. Chem. C* **2013**, *117*, 23272.
- [32] a) J. Goodwin, R. Hughes, *Rheology for chemists—An introduction. The Royal Society of Chemistry*, **2000**; b) D. Z. Gunes, R. Scirocco, J. Mewis, J. Vermant, *J. Non-Newton. Fluid.* **2008**, *155*, 39; c) S. Qazi, *PhD Thesis*, Uppsala University, **2011**.
- [33] a) D. Li, M. B. Müller, S. Gilje, R. B. Kaner, G. G. Wallace, *Nat. Nanotechnol.* **2008**, *3*, 101; b) S. Pei, H.-M. Cheng, *Carbon* **2012**, *50*, 3210; c) K. Krishnamoorthy, M. Veerapandian, K. Yun, S. J. Kim, *Carbon* **2013**, *53*, 38.
- [34] M. Matsumoto, Y. Saito, C. Park, T. Fukushima, T. Aida, *Nat. Chem.* **2015**, *7*, 730.
- [35] C. Bommier, D. Mitlin, X. Ji, *Prog. Mater Sci.* **2018**, *97*, 170.
- [36] G. M. Peng, M. Volokh, J. Tzadikov, J. W. Sun, M. Shalom, *Adv. Energy. Mater.* **2018**, *8*, 7.
- [37] M. Leskes, G. Kim, T. Liu, A. L. Michan, F. Aussenac, P. Dorffer, S. Paul, C. P. Grey, *J. Phys. Chem. Lett.* **2017**, *8*, 1078.

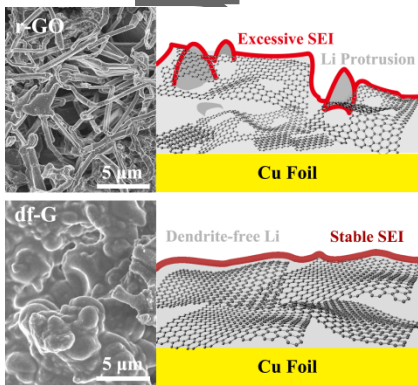
- [38] a) S. Park, R. S. Ruoff, *Nat. Nano.* **2009**, *4*, 217; b) A. Bagri, C. Mattevi, M. Acik, Y. J. Chabal, M. Chhowalla, V. B. Shenoy, *Nat. Chem.* **2010**, *2*, 581; c) S. Stankovich, D. A. Dikin, R. D. Piner, K. A. Kohlhaas, A. Kleinhammes, Y. Jia, Y. Wu, S. T. Nguyen, R. S. Ruoff, *Carbon* **2007**, *45*, 1558.
- [39] S. H. Dave, C. Gong, A. W. Robertson, J. H. Warner, J. C. Grossman, *ACS Nano* **2016**, *10*, 7515.
- [40] a) Z. Y. Xia, S. Pezzini, E. Treossi, G. Giambastiani, F. Corticelli, V. Morandi, A. Zanelli, V. Bellani, V. Palermo, *Adv. Funct. Mater.* **2013**, *23*, 4684; b) L. Zhang, Z. Zhang, C. He, L. Dai, J. Liu, L. Wang, *ACS Nano* **2014**, *8*, 6663; c) S. Haar, M. Bruna, J. X. Lian, F. Tomarchio, Y. Olivier, R. Mazzaro, V. Morandi, J. Moran, A. C. Ferrari, D. Beljonne, A. Ciesielski, P. Samorì, *J. Phys. Chem. Lett.* **2016**, *7*, 2714; d) K. Parvez, Z.-S. Wu, R. Li, X. Liu, R. Graf, X. Feng, K. Müllen, *J. Am. Chem. Soc.* **2014**, *136*, 6083; e) S. Yang, S. Brüller, Z.-S. Wu, Z. Liu, K. Parvez, R. Dong, F. Richard, P. Samorì, X. Feng, K. Müllen, *J. Am. Chem. Soc.* **2015**, *137*, 13927; f) A. M. Dimiev, G. Ceriotti, A. Metzger, N. D. Kim, J. M. Tour, *ACS Nano* **2016**, *10*, 274; g) K. H. Park, D. Lee, J. Kim, J. Song, Y. M. Lee, H.-T. Kim, J.-K. Park, *Nano Lett.* **2014**, *14*, 4306; h) P. He, H. Gu, G. Wang, S. Yang, G. Ding, Z. Liu, X. Xie, *Chem. Mater.* **2017**, *29*, 8578; i) B.-H. Wee, T.-F. Wu, J.-D. Hong, *ACS. Appl. Mater. Inter* **2017**, *9*, 4548.
- [41] a) S. Yin, Y. Zhang, J. Kong, C. Zou, C. M. Li, X. Lu, J. Ma, F. Y. C. Boey, X. Chen, *ACS Nano* **2011**, *5*, 3831; b) X. Li, Y. Hu, J. Liu, A. Lushington, R. Li, X. Sun, *Nanoscale* **2013**, *5*, 12607; c) Z. Li, Z. Xu, X. Tan, H. Wang, C. M. B. Holt, T. Stephenson, B. C. Olsen, D. Mitlin, *Energy Environ. Sci.* **2013**, *6*, 871; d) H. Hou, X. Qiu, W. Wei, Y. Zhang, X. Ji, *Adv. Energy. Mater.* **2017**, *7*, 1602898; e) Z. Li, C. Bommier, Z. S. Chong, Z. Jian, T. W. Surta, X. Wang, Z. Xing, J. C. Neuefeind, W. F. Stickle, M. Dolgos, P. A. Greaney, X. Ji, *Adv. Energy. Mater.* **2017**, *7*, 1602894; f) E. M. Lotfabad, J. Ding, K. Cui, A. Kohandehghan, W. P. Kalisvaart, M. Hazelton, D. Mitlin, *ACS Nano* **2014**, *8*, 7115; g) J. Xu, M. Wang, N. P. Wickramaratne, M. Jaroniec, S. Dou, L. Dai, *Adv. Mater.* **2015**, *27*, 2042.
- [42] a) J. R. Dahn, T. Zheng, Y. Liu, J. S. Xue, *Science* **1995**, *270*, 590; b) M. Noked, A. Soffer, D. Aurbach, *J. Solid State Electrochem.* **2011**, *15*, 1563.
- [43] J. Xu, J. Mahmood, Y. Dou, S. Dou, F. Li, L. Dai, J.-B. Baek, *Adv. Mater.* **2017**, *29*, 1702007.
- [44] E. Memarzadeh Lotfabad, P. Kalisvaart, A. Kohandehghan, D. Karpuzov, D. Mitlin, *J. Mater. Chem. A* **2014**, *2*, 19685.

- [45] Y. Shao, J. Xiao, W. Wang, M. Engelhard, X. Chen, Z. Nie, M. Gu, L. V. Saraf, G. Exarhos, J.-G. Zhang, J. Liu, *Nano Lett.* **2013**, *13*, 3909.
- [46] E. Markevich, G. Salitra, D. Aurbach, *ACS Energy Lett.* **2017**, *2*, 1337.
- [47] A. Pei, G. Zheng, F. Shi, Y. Li, Y. Cui, *Nano Lett.* **2017**, *17*, 1132.
- [48] a) G. Yanpeng, L. Huiqiao, Z. Tianyou, *Adv. Mater.* **2017**, *29*, 1700007; b) X.-B. Cheng, R. Zhang, C.-Z. Zhao, Q. Zhang, *Chem. Rev.* **2017**, *117*, 10403; c) D. Lin, Y. Liu, Y. Cui, *Nat. Nanotechnol.* **2017**, *12*, 194.
- [49] R. Akolkar, *J. Power Sources* **2014**, *246*, 84.
- [50] a) I. Christian, *The Theory of Transformations in Metals and Alloys*, 816, Pergamon Press, Oxford, **1965**; b) D. A. Porter, K. E. Easterling, M. Sherif, *Phase Transformations in Metals and Alloys, (Revised Reprint)*, CRC press, **2009**.
- [51] Q. Meng, B. Deng, H. Zhang, B. Wang, W. Zhang, Y. Wen, H. Ming, X. Zhu, Y. Guan, Y. Xiang, M. Li, G. Cao, Y. Yang, H. Peng, H. Zhang, Y. Huang, *Energy Storage Materials* **2019**, *16*, 419.
- [52] a) M. Bai, K. Xie, K. Yuan, K. Zhang, N. Li, C. Shen, Y. Lai, R. Vajtai, P. Ajayan, B. Wei, *Adv. Mater.* **2018**, *30*, 1801213; b) K. Yan, H.-W. Lee, T. Gao, G. Zheng, H. Yao, H. Wang, Z. Lu, Y. Zhou, Z. Liang, Z. Liu, S. Chu, Y. Cui, *Nano Lett.* **2014**, *14*, 6016.
- [53] D. Aurbach, B. Markovsky, A. Shechter, Y. Ein - Eli, H. Cohen, *J. Electrochem. Soc.* **1996**, *143*, 3809.
- [54] A. L. Michan, B. S. Parimalam, M. Leskes, R. N. Kerber, T. Yoon, C. P. Grey, B. L. Lucht, *Chem. Mater.* **2016**, *28*, 8149.
- [55] W. S. Hummers Jr, R. E. Offeman, *J. Am. Chem. Soc.* **1958**, *80*, 1339.

# *Pristine or Highly Defective? Understanding the Role of Graphene Structure for Stable Lithium Metal Plating*

## *Short Summary*

We are the first to examine the role of graphene host structure and chemistry in stabilizing lithium plating, showing that carbon defects correlate to Li dendrites and catalyzed SEI growth. Ideal host architecture not only promotes copious nucleation of the plating metal, shielding it from the electrolyte, but also essentially, the host itself is non-catalytic towards SEI formation.



Author Manuscript